

Evolution of Active Sites in Pt-Based Nanoalloy Catalysts for the Oxidation of Carbonaceous Species by Combined in Situ Infrared Spectroscopy and Total X-ray Scattering

Valeri Petkov,^{*,†} Yazan Maswadeh,[†] Aolin Lu,[‡] Shiyao Shan,[‡] Haval Kareem,[‡] Yinguang Zhao,[‡] Jin Luo,[‡] Chuan-Jian Zhong,[‡] Kevin Beyer,[§] and Karena Chapman[§]

[†]Department of Physics and Science of Advanced Materials Program, Central Michigan University, Mt. Pleasant, Michigan 48859, United States

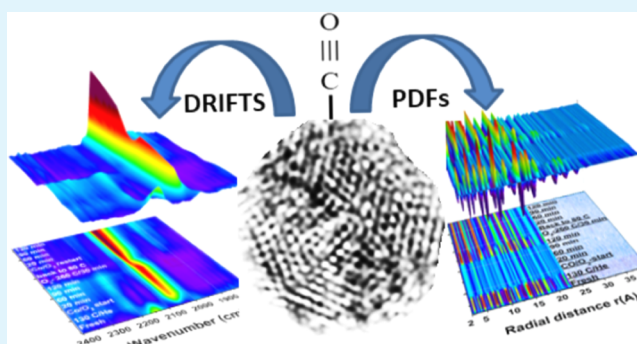
[‡]Department of Chemistry, State University of New York at Binghamton, Binghamton, New York 13902, United States

[§]X-ray Science Division, Advanced Photon Source, Argonne National Laboratory, Argonne, Illinois 60439, United States

Supporting Information

ABSTRACT: We present results from combined in situ infrared spectroscopy and total X-ray scattering studies on the evolution of catalytically active sites in exemplary binary and ternary Pt-based nanoalloys during a sequence of CO oxidation–reactivation–CO oxidation reactions. We find that when within a particular compositional range, the fresh nanoalloys may exhibit high catalytic activity for low-temperature CO oxidation. Using surface-specific atomic pair distribution functions (PDFs) extracted from the in situ total X-ray scattering data, we find that, regardless of their chemical composition and initial catalytic activity, the fresh nanoalloys suffer a significant surface structural disorder during CO oxidation. Upon reactivation in oxygen atmosphere, the surface of used nanoalloy catalysts both partially oxidizes and orders. Remarkably, it largely retains its structural state when the nanoalloys are reused as CO oxidation catalysts. The seemingly inverse structural changes of studied nanoalloy catalysts occurring under CO oxidation and reactivation conditions affect the active sites on their surface significantly. In particular, through different mechanisms, both appear to reduce the CO binding strength to the nanoalloy's surface and thus increase the catalytic stability of the nanoalloys. The findings provide clues for further optimization of nanoalloy catalysts for the oxidation of carbonaceous species through optimizing their composition, activation, and reactivation. Besides, the findings demonstrate the usefulness of combined in situ infrared spectroscopy and total X-ray scattering coupled to surface-specific atomic PDF analysis to the ongoing effort to produce advanced catalysts for environmentally and technologically important applications.

KEYWORDS: metallic nanoalloy catalysts, thermochemical treatment, CO oxidation, surface atomic structure, in situ infrared spectroscopy and total X-ray scattering



INTRODUCTION

The design of efficient catalysts for reactions involving oxidation of carbonaceous species is crucial for the development of a number of increasingly important applications, including emission control (e.g., oxidation of harmful CO in engine exhaust), off-grid power generation (e.g., oxidation of ethanol and methanol in direct alcohol fuel cells), chemical conversion (e.g., propene production from propane), and others.^{1–3} Pure Pt is the best monometallic catalyst for these applications. However, Pt is not suitable for large-scale applications because it is one of the world's rarest metals. Binary and ternary alloy nanoparticles (NPs) involving noble metals (NMs), such as Pt, Au, and Pd, and transition metals (TMs), such as Ni, Co, Fe, and Cu, have emerged as rather affordable and more active catalysts for reactions involving

oxidation of carbonaceous species as compared to pure Pt NPs.⁴ Qualitatively, the improvement is attributed to one or more of the following factors: (i) ligand/electronic effects arising from charge exchange between the NM and TM atoms, (ii) strain effects arising from the difference between the size of NM and TM atoms, and (iii) geometric effects where certain configurations of surface NM noble and TM atoms appear beneficial to the particular reaction.^{5–10} Despite the progress made, the best nanoalloy catalysts developed so far cannot quite meet the demands of practical applications. This is because, among others, the catalytically active sites on the nanoalloy's

Received: December 24, 2017

Accepted: March 13, 2018

Published: March 13, 2018

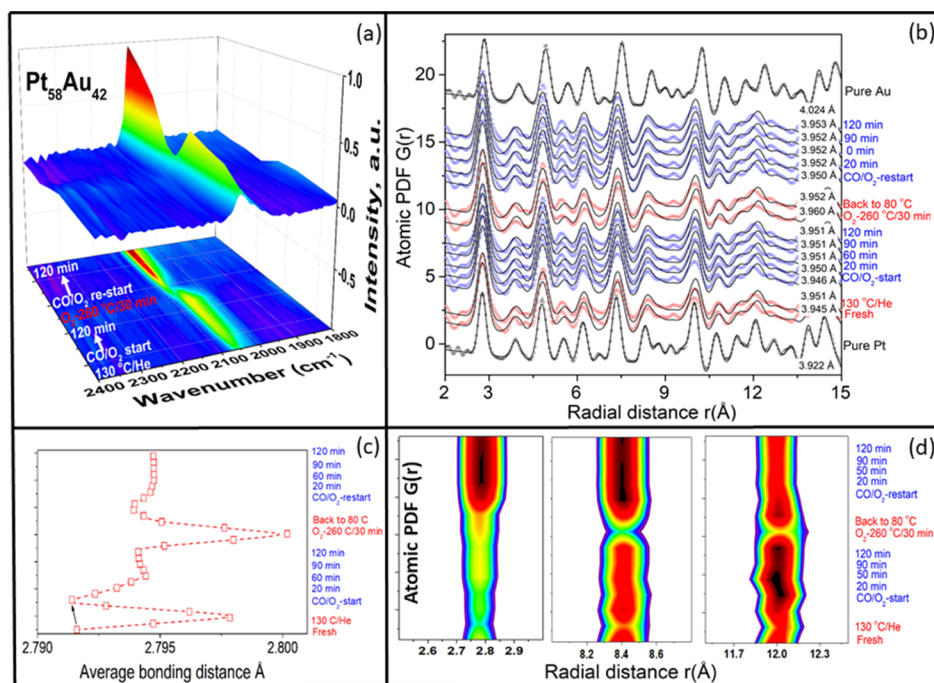


Figure 1. (a) In situ DRIFTS spectra for Pt₅₈Au₄₂ alloy NPs annealed in pure He atmosphere at 130 °C for 30 min, used as a catalyst for low-temperature (80 °C) CO oxidation for 2 h, reactivated in oxygen-rich atmosphere at 260 °C for 30 min, and then reused as a CO oxidation catalyst for 2 more hours (top panel: side view; bottom panel: top-down view). The intensity of the band appearing between 2000 and 2100 cm⁻¹ increases with changing the color from blue to dark red. (b) Concurrently obtained atomic PDFs (symbols) for the NPs. For comparison, experimental PDFs for pure Pt and Au NPs are also shown. Fits (lines) to the experimental PDFs based on fcc-type models and the refined fcc lattice parameters are shown for each PDF data set. (c) Evolution of the first-neighbor atomic distance in Pt₅₈Au₄₂ alloy NPs, as extracted from the in situ PDFs. Broken line is a guide to the eye. The arrow emphasizes the non-negligible structural relaxation of Pt₅₈Au₄₂ alloy NPs annealed in He atmosphere. (d) Color maps of three peaks in the in situ PDFs. The intensity of the peaks increases with changing the color from blue to dark red. The particular gas atmosphere, temperature, and reaction time are shown for each data set.

surface and particularly their evolution under actual reaction conditions are not well-known. It is thus imperative that the missing knowledge is obtained in an expedient and accurate manner. Here, we employ combined in situ diffuse reflection infrared Fourier transform spectroscopy (DRIFTS) and total X-ray scattering to determine the type and evolution of active sites in promising binary Pt–Au and ternary Pt–Au–Ni nanoalloy catalysts for chemical reactions involving oxidation of carbonaceous species. In particular, we study the nanoalloys under a sequence of relatively low-temperature surface cleanup (at 130 °C in He)–CO oxidation (at 80 °C)–reactivation (at 260 °C in O₂)–CO oxidation (at 80 °C) reactions lasting for 5 h in total. DRIFTS studies on nanoalloy catalysts are indeed numerous.^{11,12} Total X-ray scattering experiments on nanoalloy catalysts under reactive atmosphere, involving high-energy X-ray diffraction (HE-XRD) coupled to atomic pair distribution function (PDF) analysis, become increasingly common.^{6,13} Though very informative, combined in situ DRIFTS and total X-ray scattering studies on functioning catalysts are seldom undertaken.^{14,15} Binary NM–NM' (e.g., Pt–Au) and ternary (NM–NM'–TM) (e.g., Pt–Au–Ni) nanoalloy catalysts are considered promising for CO emission control and direct alcohol fuel cell applications.^{3,5,16,17} Besides being environmentally and technologically important, CO oxidation is also widely used as a litmus test on the performance of nanoalloy catalysts. Altogether, the in situ experimental techniques, nanoalloy catalysts, and chemical reaction probes employed here appear well-suited to pursuing the goals of our study.

EXPERIMENTAL SECTION

Nanoalloy particles were synthesized by a wet chemical route using Pt(acac)₃, Ni(acac)₂, and HAuCl₄ metal precursors. Prompted by the results of prior studies, we targeted binary nanoalloys wherein the relative Pt to Au ratio is close to 1:1 and ternary nanoalloys wherein the percentage of Pt is high, while that of Au varies greatly.^{16,17} Accordingly, the precursors were mixed in the predesired ratios and then dissolved in octadecene. The solution was heated at 230 °C for a short period of time, and then refluxed for 1 h. 1,2-Hexadecanediol was added to the solution and used as a reducing agent. Oleic acid and oleylamine were used as capping agents. The resulting nanoalloy particles were deposited on fine titania powder and activated for catalytic applications by heating at 260 °C in 20 vol % O₂ for 30 min. The activation is necessary to remove the organic molecules capping the NP surface. Besides, it stabilizes the NPs by annealing out likely atomic-level defects. More details of the synthesis and catalytic activation protocols employed here can be found in the [Supporting Information](#). Hereafter, titania-supported and activated Pt–Au and Pd–Au–Ni alloy NPs are referred to as fresh NPs.

The overall chemical composition of fresh Pt–Au and Pt–Au–Ni alloy NPs was determined by inductively coupled plasma atomic emission spectroscopy (ICP–AES) and found to be Pt₅₈Au₄₂, Pt₃₆Au₉Ni₅₅, and Pt₄₀Au₂₀Ni₄₀. The NP size and shape were determined by transmission electron microscopy (TEM). Exemplary TEM and high-resolution (HR)-TEM images of Pt₅₈Au₄₂, Pt₃₆Au₉Ni₅₅, and Pt₄₀Au₂₀Ni₄₀ NPs are shown in [Figures S1 and S2](#), respectively. As can be seen in the figures, the NPs are approximately 6.8 (±1.0) nm in size and largely spherical in shape. Besides, as lattice fringes in the HR-TEM images show, the NPs possess a good degree of crystallinity. Details of ICP–AES and TEM experiments are given in the [Supporting Information](#).

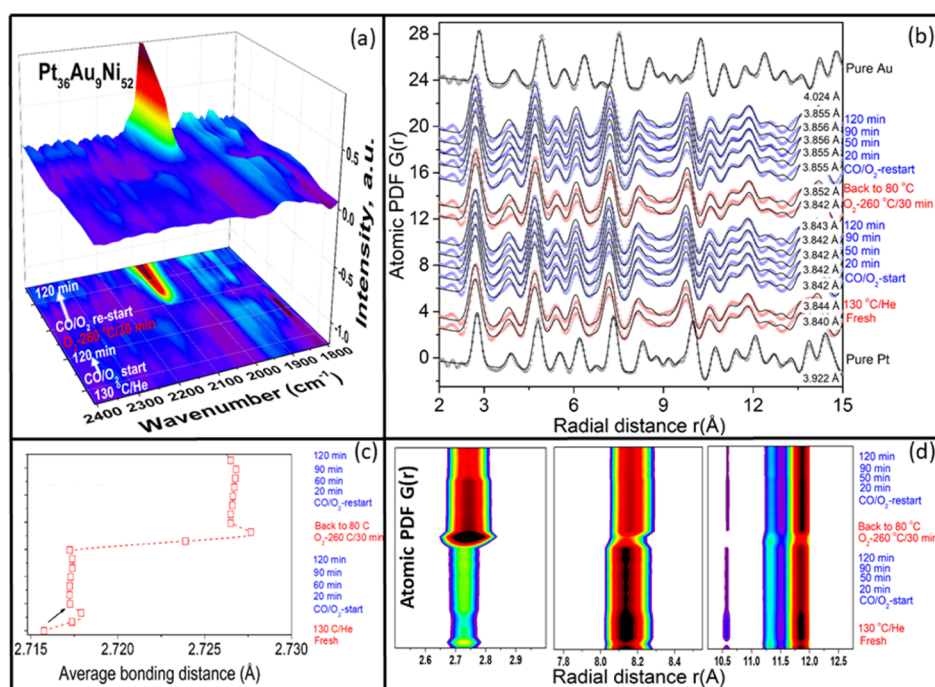


Figure 2. (a) In situ DRIFTS spectra for $\text{Pt}_{36}\text{Au}_9\text{Ni}_{52}$ alloy NPs annealed in pure He atmosphere at $130\text{ }^\circ\text{C}$ for 30 min, used as a catalyst for low-temperature ($80\text{ }^\circ\text{C}$) CO oxidation for 2 h, reactivated in oxygen-rich atmosphere at $260\text{ }^\circ\text{C}$ for 30 min, and then reused as a CO oxidation catalyst for 2 more hours (top panel: side view; bottom panel: top-down view). The intensity of the band appearing near 2100 cm^{-1} increases with changing the color from blue to dark red. (b) Concurrently obtained atomic PDFs (symbols) for the NPs. For comparison, experimental PDFs for pure Pt and Au NPs are also shown. Fits (lines) to the experimental PDFs based on fcc-type models and the refined fcc lattice parameters are shown for each PDF data set. (c) Evolution of the first-neighbor atomic distance in $\text{Pt}_{36}\text{Au}_9\text{Ni}_{52}$ alloy NPs, as extracted from the in situ PDFs. Broken line is a guide to the eye. The arrow emphasizes the non-negligible structural relaxation of $\text{Pt}_{36}\text{Au}_9\text{Ni}_{52}$ alloy NPs annealed in He atmosphere. (d) Color maps of three peaks in the in situ PDFs. The intensity of the peaks increases with changing the color from blue to dark red. The particular gas atmosphere, temperature, and reaction time are shown for each data set.

The near-surface electronic structure and chemical composition of the nanoalloy particles were determined by X-ray photoelectron spectroscopy (XPS) experiments done on a Kratos AXIS Ultra DLD spectrometer. XPS spectra showed that the individual atoms, in particular Pt and Au atoms, in the particles interact strongly, including modifying each other's electronic structure, thus confirming the formation of Pt–Au and Pt–Ni–Au nanoalloys. Besides, the spectra showed that under ambient conditions, Ni atoms in the respective nanoalloys are present as both metallic $\text{Ni}^{(0)}$ and oxidized $\text{Ni}^{(+)}$ species (see Figure S9 and Table S1). The near-surface composition of the NPs was determined from the experimental XPS spectra. Results are summarized in Table S2 together with the data for the bulk composition of the NPs obtained by ICP–AES. Analysis of the data in the table indicates that within the limits of the experimental accuracy, fresh NPs studied here are near-random alloys.

The catalytic activity of fresh $\text{Pt}_{58}\text{Au}_{42}$, $\text{Pt}_{36}\text{Au}_9\text{Ni}_{55}$, and $\text{Pt}_{40}\text{Au}_{20}\text{Ni}_{40}$ alloy NPs for the CO oxidation reaction was assessed on a custom-built system described in the Supporting Information. A representative set of CO conversion curves is shown in Figure S3. Data for the CO oxidation activity of fresh NPs are summarized in Table S3 in terms of the temperature, $T_{1/2}$, at which 50% of CO conversion (oxidation) is achieved. Values for the so-called turnover frequency (TOF), defined as $\text{TOF} = \text{number of product (CO}_2\text{) molecules per the number of active sites on the NP surface per second}$, are also shown in the table. Altogether, data in the table indicate that the catalytic activity of fresh NPs for the CO oxidation reaction increases in the order $\text{Pt}_{40}\text{Au}_{20}\text{Ni}_{40} < \text{Au}_{42}\text{Pt}_{58} < \text{Pt}_{36}\text{Au}_9\text{Ni}_{55}$, that is, it depends strongly on the nanoalloy's composition.

Combined in situ DRIFTS and total X-ray total scattering experiments on $\text{Pt}_{58}\text{Au}_{42}$, $\text{Pt}_{36}\text{Au}_9\text{Ni}_{55}$, and $\text{Pt}_{40}\text{Au}_{20}\text{Ni}_{40}$ nanoalloy catalysts were carried out using the DRIAD-X reaction cell at the beamline 11-ID-B at the Advanced Photon Source, Argonne.¹⁸ The design of the cell ensures that the infrared and X-ray beams probed

coinciding sample volumes. X-rays with an energy of 86.70 keV ($\lambda = 0.1429\text{ \AA}$) were used, and the scattered intensities were collected with a large-area detector. At first, fresh $\text{Pt}_{58}\text{Au}_{42}$, $\text{Pt}_{36}\text{Au}_9\text{Ni}_{55}$, and $\text{Pt}_{40}\text{Au}_{20}\text{Ni}_{40}$ alloy NPs were heated at $130\text{ }^\circ\text{C}$ in pure He atmosphere for 30 min to remove the gas-phase species that may have been adsorbed on their surface before the in situ experiments. The NPs were then exposed to CO oxidation conditions ($1\% \text{ CO} + 10\% \text{ O}_2$ in He) at $80\text{ }^\circ\text{C}$ for 2 h. Next, the NPs were reactivated by heating at $260\text{ }^\circ\text{C}$ in oxygen-rich atmosphere ($20\% \text{ O}_2$ in He) for 30 min. Finally, the reactivated NPs were exposed to CO oxidation conditions ($1\% \text{ CO} + 10\% \text{ O}_2$ in He) at $80\text{ }^\circ\text{C}$ for 2 more hours. DRIFTS and HE-XRD data were taken throughout the sequence of surface cleanup–CO oxidation–reactivation–CO oxidation reactions in intervals of 10 min. Evolution of in situ DRIFTS spectra for $\text{Pt}_{58}\text{Au}_{42}$, $\text{Pt}_{36}\text{Au}_9\text{Ni}_{55}$, and $\text{Pt}_{40}\text{Au}_{20}\text{Ni}_{40}$ alloy NPs during the reactions is shown in Figures 1a–3a, respectively. Exemplary in situ HE-XRD patterns are shown in Figure S5. Atomic PDFs $G(r)$ derived from the patterns are shown in Figure S6. Note that all atomic PDFs considered here are corrected for experimental artifacts and normalized in absolute units using a rigorous¹⁹ and not ad hoc²⁰ HE-XRD data reduction protocol. This facilitates the quantitative comparison between different PDF data sets described below. More details of the combined in situ DRIFTS and total X-ray scattering experiments, including derivation of atomic PDFs, can be found in the Supporting Information.

RESULTS AND DISCUSSION

Usually, the CO oxidation reaction proceeds through the so-called Langmuir–Hinshelwood (L–H) mechanism, that is, CO molecules adsorbed onto a catalyst surface react with nearby adsorbed oxygen species to form CO_2 . For clarity, the reaction path can be divided into four major steps as follows

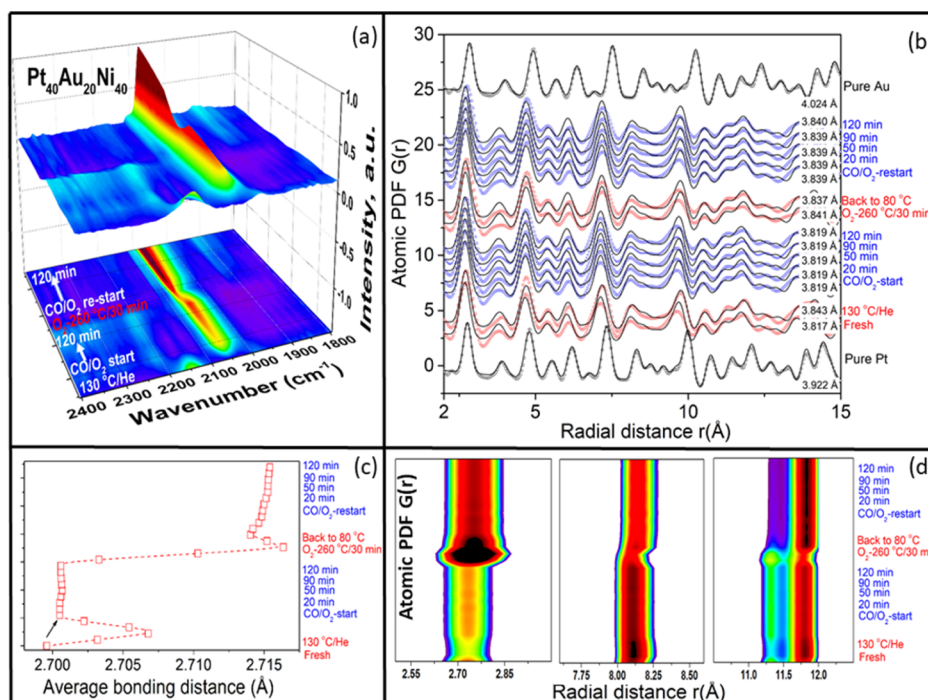
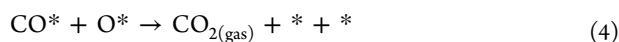
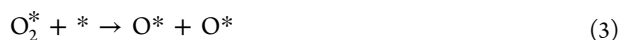


Figure 3. (a) In situ DRIFTS spectra for Pt₄₀Au₂₀Ni₄₀ alloy NPs annealed in pure He atmosphere at 130 °C for 30 min, used as a catalyst for low-temperature (80 °C) CO oxidation for 2 h, reactivated in oxygen-rich atmosphere at 260 °C for 30 min, and then reused as a CO oxidation catalyst for 2 more hours (top panel: side view; bottom panel: top-down view). The intensity of the band appearing between 2000 and 2100 cm⁻¹ increases with changing the color from blue to dark red. (b) Concurrently obtained atomic PDFs (symbols) for the NPs. For comparison, experimental PDFs for pure Pt and Au NPs are also shown. Fits (lines) to the experimental PDFs based on fcc-type models and the refined fcc lattice parameters are shown for each PDF data set. (c) Evolution of the first-neighbor atomic distance in Pt₄₀Au₂₀Ni₄₀ alloy NPs, as extracted from the in situ PDFs. Broken line is a guide to the eye. The arrow emphasizes the non-negligible structural relaxation of Pt₄₀Au₂₀Ni₄₀ alloy NPs annealed in He atmosphere. (d) Color maps of three peaks in the in situ PDFs. The intensity of the peaks increases with changing the color from blue to dark red. The particular gas atmosphere, temperature, and reaction time are shown for each data set.



where “*” stands for a surface atomic site capable of binding CO or oxygen species. The current understanding is that an efficient catalyst for CO oxidation should interact with adsorbates with ample strength so that they can react on its surface but weak enough to release the reaction intermediates and product when the reaction ends. Besides, it should allow for relatively easy dissociative adsorption of O₂.^{21–23}

On a molecular level, the adsorption of a CO molecule on an active site on the surface of the NM–metal-based catalyst may be considered in terms of concurrent transfers of charge from the filled 5σ orbital of the molecule to the surface site (σ donation) and from the surface site into the vacant (antibonding) 2π* orbitals of the molecule (π backdonation). It is also considered that the latter contributes more significantly to the adsorption energy of the molecule in comparison to the former. The bonding of a CO molecule to a surface d-metal atom, however, is best regarded as a synergistic outcome of the σ donation and π backdonation of charge. The latter increases the electron density on the molecule, which in turn facilitates the former. Notably, because the electrons in the frontier 5σ orbital of a CO molecule are largely located at the

carbon atom, the adsorption tends to occur with the carbon atom facing the catalyst’s surface. Thus, one of the most likely configurations is a CO molecule linearly (atop) adsorbed on one free surface site (step 1 of the L–H mechanism; see above). On the other hand, the adsorption of O₂ on an active surface site may be considered in terms of concurrent transfers of charge from the occupied π-bonding orbital of the molecule to the surface site (donation) and from the surface site into the empty π* orbital of the molecule (backdonation). Generally, oxygen needs two adjacent free sites for the dissociative adsorption (steps 2 and 3 of the L–H mechanism; see above). Hence, the characteristic coadsorption of CO and O₂ molecules during the CO oxidation reaction appears very different. In particular, because of the lack of available pairs of free nearby sites, oxygen dissociative adsorption may be blocked by coadsorbed CO molecules at a relatively low CO coverage of the catalyst’s surface. By contrast, there would be ample room for coadsorption of CO molecules at nearly any level of oxygen coverages.

The general understanding is that because of the partial population of antibonding 2π* orbitals taking place in the course of the σ donation/π backdonation process, the stretching frequency of the triple C≡O bond in an adsorbed CO molecule would appear diminished (“red-shifted”), as compared to CO molecules in the gas phase. Also, there is a consensus that under-coordinated surface atoms, for example, atoms occupying sharp corners (CN_{fcc} = 4 and 5), kinks (CN_{fcc} = 6), and edges (CN_{fcc} = 7) at the NP surface, would bind CO and O₂ molecules stronger than the atoms occupying highly

coordinated, planar-type surface configurations such as terraces ($CN_{fcc} = 9$). In particular, because of the increased localization of valence d-electrons and related increase in the d-electron charge density, the transfer of d-charge into the $2\pi^*$ orbital of a CO molecule adsorbed on an under-coordinated site would increase, thus strengthening the surface metal site-CO bond and weakening the triple $C\equiv O$ bond in the molecule. As a result, for CO molecules adsorbed on under-coordinated surface sites, the stretching frequency of (inner) $C\equiv O$ bonds would appear further diminished as compared to CO molecules adsorbed on highly coordinated, planar-type surface sites. For CO molecules adsorbed in the so-called “bridge” configuration involving nearby surface atoms, the stretching frequency would appear even more diminished. Conversely, an increased delocalization of valence d-electrons and related decrease in the transfer (backdonation) of d-charge into the $2\pi^*$ orbital of adsorbed CO molecules would strengthen the $C\equiv O$ bond in the molecules and lead to a relative increase (“blue shift”) in its stretching frequency. Altogether, this makes the stretching frequency of adsorbed CO molecules very sensitive to the geometry and electronic properties of the active sites on the catalyst’s surface. Note that the $C\equiv O$ bond frequency is also known to be sensitive to the surface coverage and dipole coupling between nearby adsorbed CO molecules.^{11,24} In addition, according to the theory of chemical bonding of Pauling and independent experimental studies, the elemental size of metal atoms may change upon alloying so that the ratio of the size of the alloyed atoms becomes as close to one as possible, for minimizing atomic-level stresses. Furthermore, the theory postulates and experiments confirm that changes in metal-to-metal atom bond lengths trigger changes in both the strength of the respective bonds and the electronic structure of the metal atoms involved in the bonds and vice versa. Therefore, changes in the bond lengths and electronic structure of metal atoms in (nano)alloys, including surface atoms, indeed occur concurrently and thus are difficult to take apart.^{25–27} Hence, here we consider that the ligand (charge transfer) and strain effect (bond lengths change) in nanoalloys, including the nanoalloy’s surface, largely act together and are referred to as bonding effects. For nanoalloy particles in the size range of a few nanometers, such as the NPs studied here, it is not the bonding effects that alone determine their surface atomic structure. The structure is also strongly influenced by the surface energy of metal atoms forming the NPs and interactions of surface metal atoms with the NP environment, in particular with reactive gas species.^{13,28,29}

DRIFTS spectra for fresh (cleaned up in He) $Pt_{58}Au_{42}$ and $Pt_{40}Au_{20}Ni_{40}$ alloy NPs exposed to CO oxidation reaction conditions for 2 h (see Figures 1a and 3a) show a relatively broad band of frequencies ranging from 2000 to 2100 cm^{-1} . The band is characteristic for atop adsorbed CO molecules. The band appears more intense with the latter as compared to that with the former, and, for both nanoalloys, its intensity increases with the progress of the CO oxidation reaction. Likely, under CO oxidation conditions, CO molecules keep adsorbing strongly on the surface of both fresh $Pt_{58}Au_{42}$ and $Pt_{40}Au_{20}Ni_{40}$ nanoalloys, thus diminishing the number of atomic sites that would facilitate the CO oxidation reaction. However, the number of CO molecules strongly adsorbed on the surface of the former is not as large as that in the case of the latter. DRIFTS spectra for fresh $Pt_{36}Au_9Ni_{55}$ alloy NPs exposed to CO oxidation reaction conditions for 2 h (see Figure 2a) do not show such a band. In line with the findings of catalytic ex

situ studies (see Table S1), the observation indicates that the CO oxidation reaction over the surface of fresh $Pt_{36}Au_9Ni_{55}$ alloy NPs indeed proceeds very fast. Further inspection of data in Figures 1a–3a shows that the vibrations of CO molecules linearly adsorbed on the surface of reactivated $Pt_{58}Au_{42}$ and $Pt_{40}Au_{20}Ni_{40}$ alloy NPs are shifted to higher wavenumbers. Besides, once reactivated, $Pt_{36}Au_9Ni_{55}$ nanoalloys are also seen to bind CO molecules largely in an “atop” configuration. Apparently, catalytically active surface sites in $Pt_{58}Au_{42}$, $Pt_{36}Au_9Ni_{55}$, and $Pt_{40}Au_{20}Ni_{40}$ nanoalloys evolve significantly both under CO oxidation and reactivation reaction conditions.

Analysis of the in situ atomic PDFs shown in Figures 1b–3b indicates that $Pt_{58}Au_{42}$, $Pt_{36}Au_9Ni_{55}$, and $Pt_{40}Au_{20}Ni_{40}$ alloy NPs retain their face-centered cubic (fcc)-type structure during the sequence of cleanup in He–CO oxidation–reactivation–CO oxidation reactions. However, analysis of color maps of selected peaks in the in situ PDFs indicates that the NPs indeed undergo significant changes at the atomic level, including changes in the bonding distances characteristic to the NPs (see Figures 1d–3d). The changes appear gradual during the first and second runs of the CO oxidation reaction and rather abrupt during the reactivation in oxygen atmosphere taking place in between the runs. Evolution of the average bonding (near atomic neighbor) distance in $Pt_{58}Au_{42}$, $Pt_{36}Au_9Ni_{55}$, and $Pt_{40}Au_{20}Ni_{40}$ alloy NPs with changes in the thermochemical conditions during the aforementioned sequence of reactions is shown in Figures 1c–3c, respectively. The evolution is derived from the position of peaks in the respective in situ atomic PDF data sets. As can be seen in the figures, the average bonding distance in fresh $Pt_{58}Au_{42}$ alloy NPs is approximately 2.79 Å. It appears longer than the Pt–Pt distance of 2.775 Å in pure Pt and shorter than the Au–Au distance of 2.87 Å in pure Au. In line with the finding of XPS experiments, the observation indicates that the NPs are a Pt–Au nanoalloy.³⁰ On the other hand, because of the relatively high percentage of constituent Ni atoms and relatively short Ni–Ni elemental distance (2.49 Å), the average bonding distance in fresh $Pt_{36}Au_9Ni_{55}$ and $Pt_{40}Au_{20}Ni_{40}$ alloy NPs appears in the range of 2.70–2.72 Å. That is, contrary to the case of binary $Pt_{58}Au_{42}$ alloy NPs, Pt atoms in the ternary Pt–Au–Ni NPs studied here are under considerable compressive stress. As can also be seen in the figures, bonding distances in the NPs undergo largely reversible changes during the surface cleanup in He atmosphere. In particular, as it may be expected in the case of a mild thermal treatment in inert atmosphere, the distances expand and then shrink when the NPs are, respectively, heated (130 °C) and then cooled down (room T) in He atmosphere. Furthermore, the observed reversible expansion of the average bonding distances appears to be more pronounced with $Pt_{58}Au_{42}$ alloy NPs, as compared to $Pt_{40}Au_{20}Ni_{40}$ and particularly $Pt_{36}Au_9Ni_{55}$ alloy NPs. Then, evoking the concept of structural “rigidity” of metallic alloy NPs,³¹ $Pt_{58}Au_{42}$, $Pt_{40}Au_{20}Ni_{40}$, and $Pt_{36}Au_9Ni_{55}$ alloy NPs can be considered, respectively, as “soft”, marginally “soft”, and “rigid” from a structural point of view. Note that structurally “rigid” and “soft” metallic alloy NPs would respond differently to changes in their environment, including gas-phase atmosphere and temperature.^{32–34} As discussed below, this is indeed the case with the NPs studied here. Altogether, in situ DRIFTS and structure data in Figures 1–3 indicate that relatively low-temperature gas-phase reactions in inert atmosphere, such as heating in He at 130 °C, do not affect the overall atomic arrangement in binary and ternary NM–TM nanoalloys significantly. By contrast, relatively low-temperature gas-phase

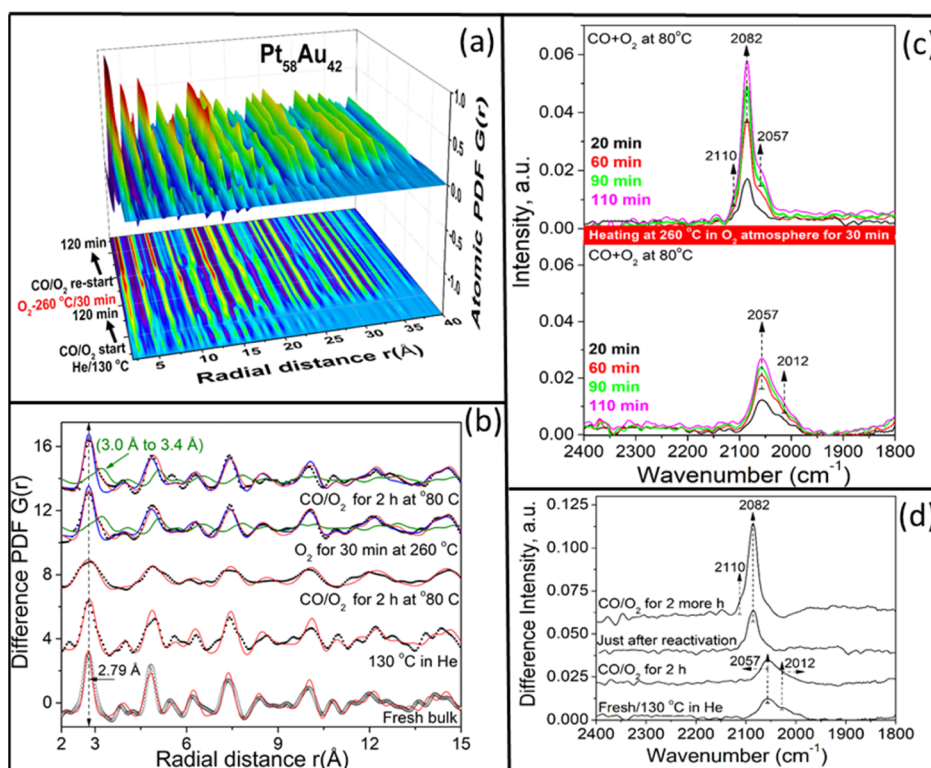


Figure 4. (a) Surface-specific atomic PDFs for $\text{Pt}_{58}\text{Au}_{42}$ alloy NPs exposed to a sequence of cleanup in He–CO oxidation–reactivation–CO oxidation reactions (top panel: side view; bottom panel: top-down view). The PDFs are derived from the in situ data sets shown in Figure 1b as explained in the text. The intensity of the PDF peaks increases with changing the color from blue to dark red. PDF peaks are seen to change in terms of both intensity and position with changes in the reaction conditions, indicating a continuous reconstruction of the surface of probed $\text{Pt}_{58}\text{Au}_{42}$ alloy NPs. (b) Selected surface-specific atomic PDFs (black symbols) from the set shown in (a). The PDFs are approximated with structure models (lines in red, blue, and green) discussed in the text. Experimental PDF for fresh $\text{Pt}_{58}\text{Au}_{42}$ alloy NPs is also given for comparison (open circles). The PDF is well-approximated with a model (red line) based on an fcc-type structure. Vertical broken line tracks the evolution of surface bonding distances in the probed $\text{Pt}_{58}\text{Au}_{42}$ alloy NPs with changes in the reaction conditions. The reaction conditions corresponding to the selected surface-specific atomic PDFs are given for each data set. (c) Selected DRIFTS spectra for the adsorption of CO molecules on the surface of probed $\text{Pt}_{58}\text{Au}_{42}$ alloy NPs. The CO oxidation exposure time is given for each data set in the respective color. Vertical broken lines mark characteristic $\text{C}\equiv\text{O}$ stretching frequencies discussed in the text (bottom panel: before reactivation; top panel: after reactivation). (d) Difference DRIFTS spectra derived from the data sets shown in (c). The spectra emphasize cumulative changes in the active surface sites in $\text{Pt}_{58}\text{Au}_{42}$ alloy NPs, as revealed by the observed cumulative changes in the $\text{C}\equiv\text{O}$ stretching frequencies.

reactions in reactive atmosphere, such as CO oxidation (at 80 °C) and reactivation in oxygen (at 260 °C), can induce significant irreversible changes in the atomic structure of the nanoalloys, including changes in the catalytically active sites on their surface.

Though indicative, structure data in Figures 1–3 are quantities averaged over the NP volume, whereas DRIFTS spectra of adsorbed CO species reflect surface structural characteristics of $\text{Pt}_{58}\text{Au}_{42}$, $\text{Pt}_{36}\text{Au}_9\text{Ni}_{55}$, and $\text{Pt}_{40}\text{Au}_{20}\text{Ni}_{40}$ alloy NPs. Hence, to reveal the observed strong impact of the reaction conditions on the catalytic properties of the NPs in better detail, we computed NP surface-specific atomic PDFs using the in situ PDF data sets. The NP surface-specific atomic PDFs for given NPs exposed to a sequence of CO oxidation–reactivation–CO oxidation conditions were computed as a difference between the respective in situ atomic PDFs and the atomic PDF for the fresh NPs. The rationale behind deriving and using surface-specific atomic PDFs is that under the conditions of aforementioned gas-phase reactions, the PDFs would largely reflect cumulative changes in the surface atomic structure of $\text{Pt}_{58}\text{Au}_{42}$, $\text{Pt}_{36}\text{Au}_9\text{Ni}_{55}$, and $\text{Pt}_{40}\text{Au}_{20}\text{Ni}_{40}$ alloy NPs occurred during the reaction sequence. Note that difference-type atomic PDFs of the type considered here have been found

advantageous in revealing structural signatures of both the metallic species intercalated in nanophase materials and gas-phase atomic species bound to the surface of metallic NPs.^{14,35} Also, note that by definition, atomic PDFs $G(r)$ considered here, including the surface-specific $G(r)$ s, oscillate about zero. The magnitude, shape, and position of the physical oscillations in the respective $G(r)$ constitute a unique structural “fingerprint” of the probed atomic configuration. Surface-specific atomic PDFs for $\text{Pt}_{58}\text{Au}_{42}$, $\text{Pt}_{36}\text{Au}_9\text{Ni}_{55}$, and $\text{Pt}_{40}\text{Au}_{20}\text{Ni}_{40}$ alloy NPs are summarized in Figures 4a–6a, respectively. The PDFs reveal that while under reaction conditions, the NPs undergo a continuous surface reconstruction. As shown below, joint analysis of selected surface-specific atomic PDFs and DRIFTS spectra helps reveal the major steps of the reconstruction and its impact on the catalytically active sites in the NPs.

In particular, as data in Figures 4b–6b indicate, $\text{Pt}_{58}\text{Au}_{42}$, $\text{Pt}_{36}\text{Au}_9\text{Ni}_{55}$, and $\text{Pt}_{40}\text{Au}_{20}\text{Ni}_{40}$ alloy NPs undergo surface relaxation alone when exposed to He atmosphere at 130 °C for 30 min. The relaxation does not seem to affect significantly the average surface bonding distance in $\text{Pt}_{58}\text{Au}_{42}$ alloy NPs (see the broken line running through the first peak in the PDF data sets shown in Figure 4b). In the case of $\text{Pt}_{40}\text{Au}_{20}\text{Ni}_{40}$ alloy NPs exposed to He atmosphere, the average surface bonding

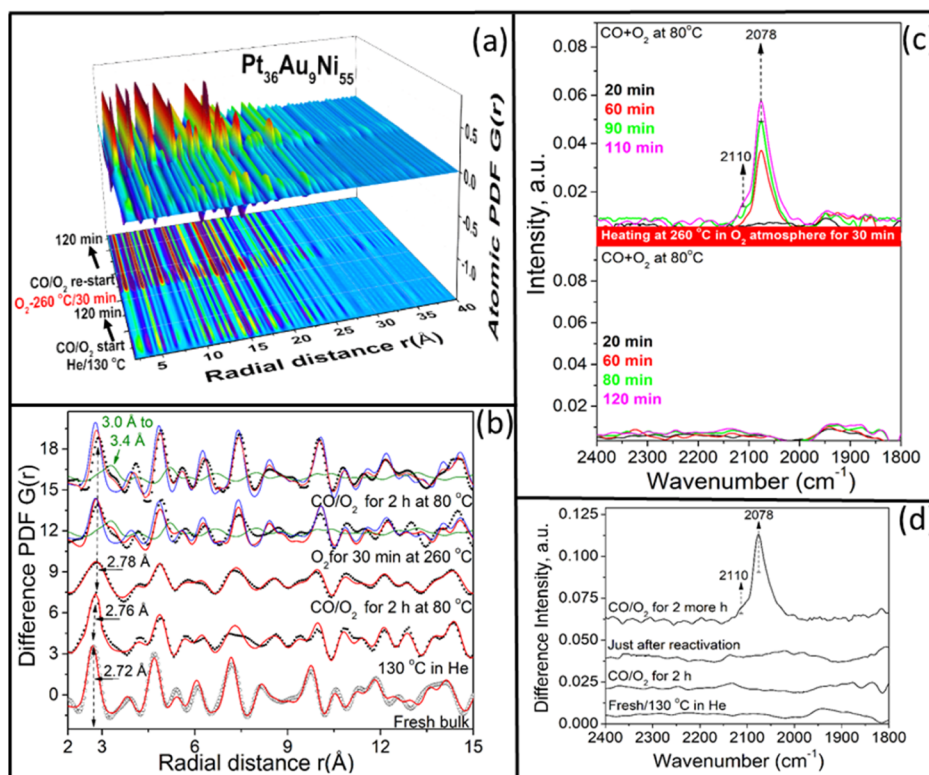


Figure 5. (a) Surface-specific atomic PDFs for $\text{Pt}_{36}\text{Au}_9\text{Ni}_{55}$ alloy NPs exposed to a sequence of cleanup in He–CO oxidation–reactivation–CO oxidation reactions (top panel: side view; bottom panel: top-down view). The PDFs are derived from the in situ data sets shown in Figure 2b as explained in the text. The intensity of the PDF peaks increases with changing the color from blue to dark red. PDF peaks are seen to change in terms of both intensity and position with changes in the reaction conditions, indicating a continuous reconstruction of the surface of probed $\text{Pt}_{36}\text{Au}_9\text{Ni}_{55}$ alloy NPs. (b) Selected surface-specific atomic PDFs (black symbols) from the set shown in (a). The PDFs are approximated with structure models (lines in red, blue, and green) discussed in the text. Experimental PDF for fresh $\text{Pt}_{36}\text{Au}_9\text{Ni}_{55}$ alloy NPs is also given for comparison (open circles). The PDF is well-approximated with a model (red line) based on an fcc-type structure. Vertical broken line tracks the evolution of surface bonding distances in the probed $\text{Pt}_{36}\text{Au}_9\text{Ni}_{55}$ alloy NPs with changes in the reaction conditions. The reaction conditions corresponding to the selected surface-specific atomic PDFs are given for each data set. (c) Selected DRIFTS spectra for the adsorption of CO molecules on the surface of probed $\text{Pt}_{36}\text{Au}_9\text{Ni}_{55}$ alloy NPs. The CO oxidation exposure time is given for each data set in the respective color. Vertical broken lines mark characteristic $\text{C}\equiv\text{O}$ stretching frequencies discussed in the text. (d) Difference DRIFTS spectra derived from the data sets shown in (c). The spectra emphasize cumulative changes in the active surface sites in $\text{Pt}_{36}\text{Au}_9\text{Ni}_{55}$ alloy NPs, as revealed by the observed cumulative changes in the $\text{C}\equiv\text{O}$ stretching frequencies.

distance expands from 2.70 to 2.76 Å, that is, toward the elemental Pt–Pt bonding distance (see the arrows in Figure 6b). The expansion would diminish significantly the compressive atomic-level stresses at the NP surface. In the case of $\text{Pt}_{36}\text{Au}_9\text{Ni}_{55}$ alloy NPs exposed to He atmosphere, the expansion of the average surface bonding distance from 2.72 to 2.76 Å (see the arrows in Figure 5b) and thus the diminishing of the compressive atomic-level stresses at the NP surface are also significant. After exposure to CO oxidation conditions for 2 h, the cleaned-up (in He) surface of $\text{Pt}_{58}\text{Au}_{42}$, $\text{Pt}_{36}\text{Au}_9\text{Ni}_{55}$, and $\text{Pt}_{40}\text{Au}_{20}\text{Ni}_{40}$ alloy NPs appears very disordered at the atomic level. The disorder is clearly revealed by the overall smearing of the oscillations (peaks) in the respective surface-specific atomic PDFs. The degree of surface disorder appears larger with the structurally “soft” $\text{Pt}_{58}\text{Au}_{42}$ alloy NPs as compared to the case of structurally “rigid” $\text{Pt}_{40}\text{Au}_{20}\text{Ni}_{40}$ and $\text{Pt}_{36}\text{Au}_9\text{Ni}_{55}$ alloy NPs (compare the widths of the peaks in the respective surface-specific atomic PDFs). Besides, the average surface bonding distance in the latter expands further. When reactivated at 260 °C in oxygen-rich atmosphere for 30 min, $\text{Pt}_{58}\text{Au}_{42}$, $\text{Pt}_{36}\text{Au}_9\text{Ni}_{55}$, and $\text{Pt}_{40}\text{Au}_{20}\text{Ni}_{40}$ alloy NPs undergo significant surface oxidation. Likely, the oxidation involves both chemisorbed individual oxygen species and formation of well-

structured oxide islands/layer(s). The latter is signified by the appearance of metal-to-metal atom distances (see the green arrows in Figures 4b–6b) characteristic to cubic-like NiO and/or tetragonal-like PtO.³⁶ Fragments from the structures are shown in Figure S7. Besides, as data in Figures 4b–6b show, the low- r part of the surface-specific PDFs for the reactivated NPs, extending from r values of 2.5 to about 15–20 Å, is approximated best by a model (red line) featuring a mixture of (blue line) fcc-type packed metal atoms and (green line) oxidized metal species ($\text{Ni}^{(2+)}\text{—O}/\text{Pt}^{(2+)}\text{—O}$). Note that other studies have also indicated the formation of a thin tetragonal-like PtO and not trigonal-like $\alpha\text{-PtO}_2$ layer on Pt surfaces exposed to oxygen atmosphere and/or CO oxidation conditions at moderate temperature.³⁷ The degree of oxidation is seen to increase in the order $\text{Pt}_{36}\text{Au}_9\text{Ni}_{55} < \text{Pt}_{58}\text{Au}_{42} \approx \text{Pt}_{40}\text{Au}_{20}\text{Ni}_{40}$ alloy NPs. On the basis of the chemical composition of the NPs, results of XPS experiments, oxophilicity of the respective metallic species,³⁸ and prior work,^{3,8,39} it may be conjectured that the surface oxidation of reactivated $\text{Pt}_{58}\text{Au}_{42}$ alloy NPs involves Pt–O species alone, whereas both Pt–O and Ni–O species coexist on the surface of reactivated $\text{Pt}_{36}\text{Au}_9\text{Ni}_{55}$ and $\text{Pt}_{40}\text{Au}_{20}\text{Ni}_{40}$ alloy NPs. Notably, though diminished in numbers, the surface metal–oxide species

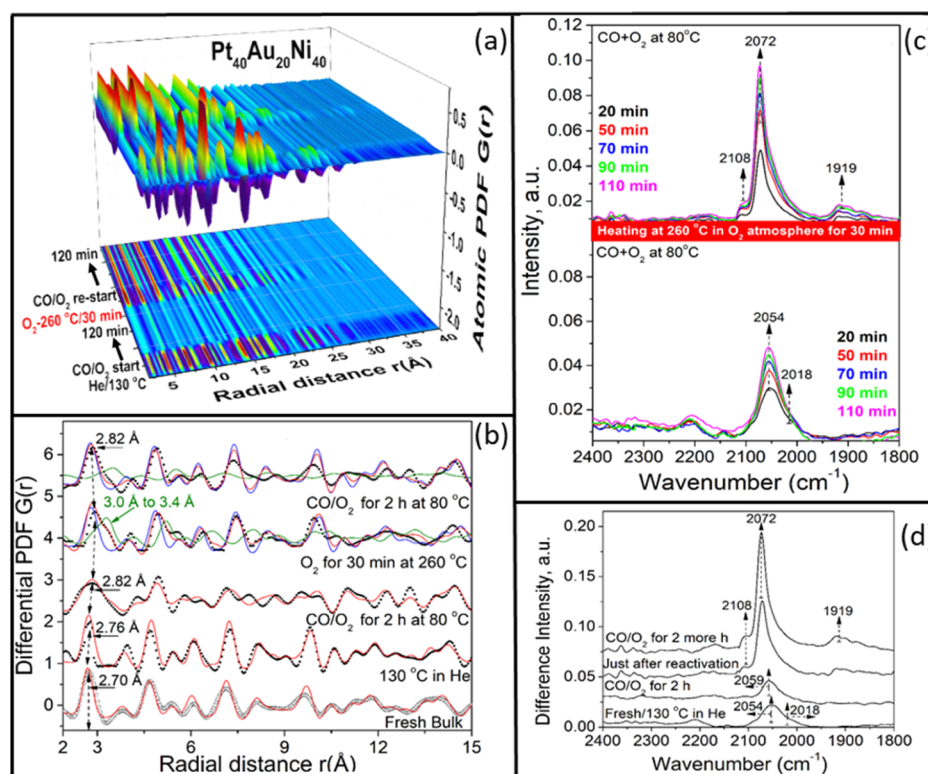


Figure 6. (a) Surface-specific atomic PDFs for $\text{Pt}_{40}\text{Au}_{20}\text{Ni}_{40}$ alloy NPs exposed to a sequence of cleanup in He–CO oxidation–reactivation–CO oxidation reactions (top panel: side view; bottom panel: top-down view). The PDFs are derived from the in situ data sets shown in Figure 3b as explained in the text. The intensity of the PDF peaks increases with changing the color from blue to dark red. PDF peaks are seen to change in terms of both intensity and position with changes in the reaction conditions, indicating a continuous reconstruction of the surface of probed $\text{Pt}_{40}\text{Au}_{20}\text{Ni}_{40}$ alloy NPs. (b) Selected surface-specific atomic PDFs (black symbols) from the set shown in (a). The PDFs are approximated with structure models (lines in red, blue, and green) discussed in the text. Experimental PDF for fresh $\text{Pt}_{40}\text{Au}_{20}\text{Ni}_{40}$ alloy NPs is also given for comparison (open circles). The PDF is well-approximated with a model (red line) based on an fcc-type structure. Vertical broken line tracks the evolution of surface bonding distances in the probed $\text{Pt}_{40}\text{Au}_{20}\text{Ni}_{40}$ alloy NPs with changes in the reaction conditions. The reaction conditions corresponding to the selected surface-specific atomic PDFs are given for each data set. (c) Selected DRIFTS spectra for adsorption of CO molecules on the surface of probed $\text{Pt}_{40}\text{Au}_{20}\text{Ni}_{40}$ alloy NPs. The CO oxidation exposure time is given for each data set in the respective color. Vertical broken lines mark characteristic $\text{C}\equiv\text{O}$ stretching frequencies discussed in the text. (d) Difference DRIFTS spectra derived from the data sets shown in (c). The spectra emphasize cumulative changes in the active surface sites in $\text{Pt}_{40}\text{Au}_{20}\text{Ni}_{40}$ alloy NPs, as revealed by the observed cumulative changes in the $\text{C}\equiv\text{O}$ stretching frequencies.

do not disappear completely when the reactivated NPs are reused as CO oxidation catalysts for 2 more hours. However, the surface of reused alloy NPs seems to evolve toward a more ordered structural state with the progress of CO oxidation (compare the width of the first peak in the surface-specific PDFs for fresh, used, reactivated, and then further used nanoalloy catalysts shown in Figures 4b–6b).

Selected DRIFTS and difference DRIFTS spectra for $\text{Pt}_{58}\text{Au}_{42}$, $\text{Pt}_{36}\text{Au}_9\text{Ni}_{55}$, and $\text{Pt}_{40}\text{Au}_{20}\text{Ni}_{40}$ alloy NPs exposed to CO oxidation–reactivation–CO oxidation conditions are shown in Figures 4c,d–6c,d respectively. The latter were computed as a difference between the respective in situ DRIFTS data sets and the DRIFTS spectrum for the fresh NPs. Under the evolving conditions of aforementioned gas-phase reactions, the so-computed difference DRIFTS spectra would emphasize cumulative changes in the active sites on the surface of $\text{Pt}_{58}\text{Au}_{42}$, $\text{Pt}_{36}\text{Au}_9\text{Ni}_{55}$, and $\text{Pt}_{40}\text{Au}_{20}\text{Ni}_{40}$ alloy NPs that occurred during the reaction sequence.

As data in Figure 5c,d show, virtually no CO molecules bind strongly to the surface of fresh $\text{Pt}_{36}\text{Au}_9\text{Ni}_{55}$ alloy NPs exposed to CO oxidation conditions. In line with the findings of ex situ catalytic studies, the observation indicates that the rate of CO oxidation over the NPs is high. Taking into consideration

results from the analysis of respective surface-specific atomic PDFs, the superb catalytic activity of $\text{Pt}_{36}\text{Au}_9\text{Ni}_{55}$ alloy NPs for the CO oxidation reaction can be attributed to the fact that surface Pt atoms in the NPs largely remain under compressive stress (the average surface bonding distances remain ≤ 2.78 Å; see Figure 5b) throughout the reaction. The stress would lead to a downshift of the d-band and diminish the density of states of valence d-electrons of surface Pt sites that are available for backdonation into the $2\pi^*$ orbitals of CO molecules adsorbed on the sites. Eventually, this would weaken the binding energy of the molecules and thus accelerate their oxidation into CO_2 . On the basis of the chemical composition of the NPs and results of prior studies,^{3,39} it may be conjectured that by exchanging charge with the majority Pt atoms (see Figure S9), the minority Au atoms in $\text{Pt}_{36}\text{Au}_9\text{Ni}_{55}$ alloy NPs may facilitate but not fully determine the kinetics of CO oxidations over the NPs. Though to a lesser extent, the same pertains to fresh $\text{Pt}_{58}\text{Au}_{42}$ and $\text{Pt}_{40}\text{Au}_{20}\text{Ni}_{40}$ alloy NPs wherein Au species are also the minority species. The likely transfer of charge from the less electronegative Ni atoms (1.9) to the more electronegative Pt atoms (2.2) in $\text{Pt}_{36}\text{Au}_9\text{Ni}_{55}$ alloy NPs may be another important factor behind their superb CO oxidation activity.^{5,39} Note that the catalytic synergy between surface NM and TM

species in fresh Pt₄₀Au₂₀Ni₄₀ alloy NPs appears less well-expressed as compared to that observed with fresh Pt₃₆Au₉Ni₅₅ alloy NPs because, contrary to the case with the latter, the average surface bonding distance in the former is seen to increase well above 2.78 Å during the CO oxidation reaction. The resulting tensile stresses would sharpen and uplift the d-band of surface Pt atoms in Pt₄₀Au₂₀Ni₄₀ alloy NPs, thereby disturbing the exchange of charge between the adsorbed CO molecules and respective surface sites (i.e., disturbing the σ donation and π backdonation synergy discussed above).

As can be seen in Figures 4c,d and 6c,d, CO vibration frequencies in the DRIFTS spectra of fresh Pt₅₈Au₄₂ and Pt₄₀Au₂₀Ni₄₀ alloy NPs form a broad band with a major peak at about 2054–2057 cm⁻¹ and a shoulder at about 2012–2018 cm⁻¹. The peak can be attributed to CO molecules adsorbed atop Pt atoms from planar-type surface configurations such as (111)_{fcc} terraces. The shoulder can be attributed to CO molecules adsorbed atop corrugated terraces and kinks formed of surface Pt atoms. Notably, no CO vibration frequencies at 2170 cm⁻¹ that are characteristic to CO molecules adsorbed on titania are observed.^{40–43} Further inspection of the figures shows that the CO accumulation on the surface of fresh Pt₅₈Au₄₂ and Pt₄₀Au₂₀Ni₄₀ alloy NPs does not reach saturation under the particular CO oxidation conditions. The likely reason is that according to the Langmuir–Hinshelwood mechanism, the CO oxidation reaction involves molecular and dissociative adsorption of CO and O₂ molecules, respectively, and a consequent diffusion of adsorbed CO molecules toward oxygen atoms occupying nearby surface sites, followed by the production of CO₂, which rapidly vacates the surface. The diffusion of CO would induce a significant surface structural disorder, as indeed observed here (see the respective surface-specific atomic PDFs shown in Figures 4b and 6b). Experimental studies of others on monocrystal Pt surfaces and fine Pt NPs exposed to CO have arrived at the same conclusion.^{28,44} Additional active sites involving Pt species would be created in the course of surface disordering and exposed to CO oxidation conditions, including sites from subsurface atomic layers. The sites would favor dissociative adsorption of O₂ and/or consume gas-phase CO species, thus maintaining the CO oxidation reaction as observed here.

Studies have shown that at near room temperature, CO molecules tend to adsorb firmly on Pt surface sites and thus do not diffuse inside Pt-based nanoalloy catalysts. By contrast, oxygen atoms diffuse relatively easily into the bulk of Pt-based nanoalloy catalysts, thus forming disordered nonstoichiometric surface oxides.^{43–47} As the respective surface-specific atomic PDFs show, the latter are clearly present on the surface of reactivated Pt₅₈Au₄₂, Pt₃₆Au₉Ni₅₅, and Pt₄₀Au₂₀Ni₄₀ alloy NPs. Furthermore, as the in situ DRIFTS and particularly difference DRIFTS spectra clearly show, the oxides affect the active sites on the NP surface considerably. In particular, DRIFTS spectra for reactivated Pt₅₈Au₄₂ and Pt₄₀Au₂₀Ni₄₀ alloy NPs (see Figures 4c and 6c) appear dominated by a well-defined peak at 2082 and 2072 cm⁻¹, respectively. The peak can be attributed to CO molecules adsorbed atop highly coordinated Pt surface sites such as terraces. In the case of reactivated Pt₅₈Au₄₂ alloy NPs, the dominant peak has a shoulder at 2057 cm⁻¹. As the respective difference DRIFTS spectrum shows, the shoulder can be attributed to CO molecules adsorbed atop surface sites inherited from the fresh NPs. The peak-to-shoulder intensity ratio does not change much during the CO oxidation reaction, which indicates that the newly created and the inherited surface

sites are indeed well-defined and not much related to each other. In the case of reactivated Pt₄₀Au₂₀Ni₄₀ alloy NPs, the dominant peak at 2072 cm⁻¹ appears highly asymmetric with a tail extending to CO stretching frequencies as low as 2000 cm⁻¹. The tail indicates that upon reactivation, the surface of the Pt₄₀Au₂₀Ni₄₀ nanoalloy catalyst becomes rich in various under-coordinated Pt sites known to bind (atop) CO molecules stronger in comparison to sites on smooth Pt surfaces. Besides, DRIFTS spectra for reactivated Pt₄₀Au₂₀Ni₄₀ alloy NPs show CO stretching frequencies clustered at approximately 1919 cm⁻¹, which can be attributed to CO molecules adsorbed on “bridge” sites. The stretching frequencies characteristic to CO molecules bound atop under-coordinated and “bridge” sites persist during the CO oxidation reaction, indicating that the surface of reactivated Pt₄₀Au₂₀Ni₄₀ alloy NPs remains rough and thus rather reactive under the particular CO oxidation conditions. Upon reactivation, the surface of the Pt₃₆Au₉Ni₅₅ nanoalloy catalyst is also seen to evolve considerably and start interacting more strongly with CO species in comparison to that of the fresh catalyst. In particular, as data in Figure 5c,d show, CO molecules appear bound preferably atop highly coordinated sites on smooth terraces at the nanoalloy's surface.

DRIFTS spectra in Figures 4c,d–6c,d also show that similar to the case of fresh NPs, the CO accumulation on the surface of reactivated Pt₅₈Au₄₂, Pt₃₆Au₉Ni₅₅, and Pt₄₀Au₂₀Ni₄₀ alloy NPs does not reach saturation under the particular CO oxidation conditions. While an increased surface structural disorder and related generation of additional active sites may account for the catalytic stability of the fresh nanoalloys, partial surface oxidation seems to be the reason behind the observed catalytic stability of the reactivated nanoalloys. In particular, the preadsorbed oxygen species would withdraw charge from the neighboring Pt atoms, thereby diminishing their ability to (back)donate charge to the 2 π^* orbitals of coadsorbed CO molecules.^{48–50} The likeliness of this scenario is evidenced by the diminished “red shift”/relative “blue shift” (~20 cm⁻¹) of the major peaks in the DRIFTS spectra of the reactivated nanoalloys in comparison to the fresh nanoalloys (see Figures 4c,d and 6c,d). The likely presence of partial positive charge on surface Pt atoms in the reactivated nanoalloys is also indicated by the presence of CO stretching frequencies at 2008–2010 cm⁻¹ in the respective DRIFTS spectra. The frequencies appear despite the percentage of Au (and Ni species) in the nanoalloys being low or high and persist over 2 h under the particular CO oxidation conditions, indicating that the preadsorbed oxygen species are at least partially replenished during the reaction. Surface-specific atomic PDFs for the reactivated nanoalloys also indicate the likely presence of surface Pt–O species throughout the CO oxidation reaction. It is noteworthy that the presence of preadsorbed oxygen species would limit the diffusion of CO molecules over the surface of reactivated nanoalloys, thus limiting its eventual disordering during the reaction. The latter is a fact, as the respective surface-specific atomic PDFs show (see Figures 4b–6b).

CONCLUSIONS

As once again demonstrated here, the activity of as-synthesized and activated NM–TM nanoalloy catalysts (NMs = Pt and Au and TM = Ni) for the oxidation of carbonaceous species, in particular CO, depends strongly on the nanoalloy's composition. However, the nanoalloy's surface and thus catalytically active sites in the nanoalloys evolve significantly both under reaction and reactivation conditions. In particular, the surface of

just activated nanoalloys exposed to CO oxidation conditions suffers a significant structural disorder. The disorder scales with the structural “softness” of the particular nanoalloys. Likely, it is facilitated by the “softening” of surface metal-to-metal atom bonds because of the transfer of charge from the atoms (backdonation) into the vacant (antibonding) $2\pi^*$ orbitals of CO molecules bound to the atoms. Besides, it is likely to be facilitated by the tendency of adsorbed CO molecules to distance from each other through diffusion over the nanoalloy’s surface, for minimizing the molecular dipole–dipole interactions. In the process, additional active sites may be created, including sites from subsurface atomic layers, thereby improving the catalytic stability of the nanoalloys. Notably, despite being carried out under the same thermochemical conditions (treatment in oxygen-rich atmosphere at 260 °C), the initial activation of fresh and reactivation of used NM–TM nanoalloy catalysts affect their surface in a significantly different way. In particular, as the surface-specific atomic PDFs show, the activation does not result in a significant oxidation of the nanoalloy’s surface, whereas the reactivation results in a significant oxidation of the nanoalloy’s surface. Likely, the oxidation is facilitated by the presence of a significant structural disorder at the surface of used nanoalloys, whereas the concurrent diminishing of the latter is temperature-driven. The preadsorbed oxygen species make the active sites on the surface of reused nanoalloys less prone to exchange charge with adsorbed CO molecules, as indicated by the observed overall reduction of the “red shift” in the stretching frequencies of adsorbed CO molecules. This reduces the poisoning effect of adsorbed CO molecules, thereby increasing the catalytic stability of the nanoalloys. Moreover, depending on the nanoalloy’s composition and pretreatment, adsorbed CO molecules may be displaced to significantly different active sites, including “bridge sites”, opening new channels for the catalytic oxidation of CO.

Generally, albeit the chemical composition of nanoalloys explored for catalytic applications is readily available, it may be difficult to predict and thus achieve control over the evolution of active sites on the surface of functioning fresh and/or reactivated nanoalloy catalysts. Combined in situ DRIFTS and total X-ray scattering experiments, including surface-specific atomic PDF analysis, can be very helpful in this respect by providing a feedback loop for designing nanoalloy catalysts with better activity and stability. For example, the studies presented here show that $\text{Pt}_{36}\text{Au}_9\text{Ni}_{55}$ nanoalloys are superior to $\text{Pt}_{40}\text{Au}_{20}\text{Ni}_{40}$ nanoalloys in terms of catalytic activity for low-temperature CO oxidation. This is because the CO adsorption is somewhat stronger on the surface of the latter as compared to that of the former. However, the propensity of both activated and reactivated $\text{Pt}_{40}\text{Au}_{20}\text{Ni}_{40}$ nanoalloys to bind CO molecules stronger than other members of the family of Pt–Au and Pt–Au–Ni nanoalloys do indicates that they may be excellent catalysts for other chemical reactions. In particular, $\text{Pt}_{40}\text{Au}_{20}\text{Ni}_{40}$ nanoalloys may promote the oxidation of ethanol in direct alcohol fuel cells, where a somewhat stronger CO binding energy to the catalyst’s surface helps split C–C bonds and remove CO intermediates via the production of CO_2 . Our recent studies confirm that this is indeed the case.⁵¹ Last but not least, our very recent combined in situ DRIFTS and total X-ray scattering experiments indicate that the technique can be useful in studies of nanoalloy catalysts for other technologically important gas-phase reactions such as low-temperature oxidation of propane.⁵²

■ ASSOCIATED CONTENT

Supporting Information

The Supporting Information is available free of charge on the ACS Publications website at DOI: 10.1021/acsami.7b19574.

Synthesis protocol, details of the in situ total scattering experiments, TEM images, and XPS spectra (PDF)

■ AUTHOR INFORMATION

Corresponding Author

*E-mail: petko1vg@cmich.edu.

ORCID

Valeri Petkov: 0000-0002-6392-7589

Chuan-Jian Zhong: 0000-0003-0746-250X

Karena Chapman: 0000-0002-8725-5633

Notes

The authors declare no competing financial interest.

■ ACKNOWLEDGMENTS

This work was supported by DOE-BES grant DE-SC0006877 and in part by NSF (CHE 1566283). Also, it used resources of the Advanced Photon Source at the Argonne National Laboratory provided by the DOE Office of Science under contract no. DE-AC02-06CH11357. Thanks are due to Dr. B. Prasai for the help with the HE-XRD experiments and data processing.

■ REFERENCES

- (1) Twigg, M. V. Catalytic Control of Emissions from Cars. *Catal. Today* **2011**, *163*, 33–41.
- (2) Süslü, O. S.; Becerik, I. On-board Fuel Processing for a Fuel cell–heat Engine Hybrid System. *Energy Fuels* **2009**, *23*, 1858–1873.
- (3) Zhong, C. J.; Luo, J.; Fang, B.; Wanjala, B. N.; Njoki, P. N.; Loukrakpam, R.; Yin, J. Nanostructured Catalysts in Fuel Cells. *Nanotechnology* **2010**, *21*, 062001–062020.
- (4) Note, following the widely adopted definition (e.g., see: Callister, W. D. *Materials Science and Engineering: An Introduction*; John Wiley & Sons: New York, 2007), throughout the paper the term “alloy” is used to describe any mixture of distinct metallic species, irrespective of the degree of their mixing and way of mixing.
- (5) Loukrakpam, R.; Yuan, Q.; Petkov, V.; Gan, L.; Rudi, S.; Yang, R.; Huang, Y.; Brankovic, S. R.; Strasser, P. Efficient C–C bond Splitting on Pt Monolayer and Sub-Monolayer Catalysts During Ethanol Electro-Oxidation: Pt Layer Strain and Morphology Effects. *Phys. Chem. Chem. Phys.* **2014**, *16*, 18866–18876.
- (6) Shan, S.; Petkov, V.; Yang, L.; Luo, J.; Joseph, H.; Mayzel, D.; Prasai, B.; Wang, L.; Engelhard, M.; Zhong, C. J. Atomic-Structural Synergy for Catalytic CO Oxidation over Palladium–Nickel Nanoalloys. *J. Am. Chem. Soc.* **2014**, *136*, 7140–7151.
- (7) Shan, S.; Petkov, V.; Yang, L.; Mott, D.; Wanjala, B. N.; Cai, F.; Chen, B. H.; Luo, J.; Zhong, C.-J. Oxophilicity and Structural Integrity in Maneuvering Surface Oxygenated Species on Nanoalloys for CO oxidation. *ACS Catal.* **2013**, *13*, 3075–3085.
- (8) Cuenya, B. R.; Behafarid, F. Nanocatalysis: Size- and Shape-Dependent Chemisorption and Catalytic reactivity. *Surf. Sci. Rep.* **2015**, *70*, 135–187.
- (9) Hammer, B.; Nørskov, J. K. Theoretical Surface Science and Catalysis—Calculations and Concepts. *Adv. Catal.* **2000**, *45*, 71–129.
- (10) Mavrikakis, M.; Hammer, B.; Nørskov, J. K. Effect of Strain on the Reactivity of Metal Surfaces. *Phys. Rev. Lett.* **1998**, *13*, 2819–2822.
- (11) Zaera, F. New Advances in the Use of Infrared absorption Spectroscopy for the Characterization of Heterogeneous Catalytic Reactions. *Chem. Soc. Rev.* **2014**, *43*, 7624–7663.

- (12) Ye, J.-Y.; Jiang, Y.-X.; Sheng, T.; Sun, S.-G. In-situ FTIR Spectroscopic Studies of Electrocatalytic Reactions and Processes. *Nano Energy* **2016**, *29*, 414–427.
- (13) Petkov, V.; Yang, L.; Yin, J.; Loukrakpam, R.; Shan, S.; Wanjala, B.; Luo, J.; Chapman, K. W.; Zhong, C. J. Reactive Gas Environment Induced structural Modification of Noble-Transition Metal alloy Nanoparticles. *Phys. Rev. Lett.* **2012**, *109*, 125504.
- (14) Newton, M. A.; Chapman, K. W.; Thompsett, D.; Chupas, P. J. Chasing Changing Nanoparticles with Time-Resolved Pair Distribution Function Methods. *J. Am. Chem. Soc.* **2012**, *134*, 5036–5039.
- (15) Hanson, J. C.; Si, R.; Xu, W.; Senanayake, S. D.; Mudiyansele, K.; Stacchiola, D.; Rodriguez, J. A.; Zhao, H.; Beyer, K. A.; Jennings, G.; Chapman, K. W.; Chupas, P. G.; Martínez-Arias, A. Pulsed-Reactant in situ Studies of Ceria/CuO Catalysts Using Simultaneous XRD, PDF and DRIFTS Measurements. *Catal. Today* **2014**, *229*, 64–71.
- (16) Koh, S.; Toney, M. F.; Strasser, P. Activity–stability relationships of ordered and disordered alloy phases of Pt₃Co electrocatalysts for the oxygen reduction reaction (ORR). *Electrochim. Acta* **2007**, *170*, 2765–2774.
- (17) Loukrakpam, R.; Luo, J.; He, T.; Chen, Y.; Xu, Z.; Njoki, P. N.; Wanjala, B. N.; Fang, B.; Mott, D.; Yin, J.; Klar, J.; Powell, B.; Zhong, C. J. Nanoengineered PtCo and PtNi Catalysts for Oxygen Reduction Reaction: an Assessment of the Structural and Electrocatalytic Properties. *J. Phys. Chem. C* **2011**, *115*, 1682–1694.
- (18) Beyer, K. A.; Zhao, H.; Borkiewicz, O. J.; Newton, M. A.; Chupas, P. J.; Chapman, K. W. Simultaneous Diffuse Reflection Infrared Spectroscopy and X-ray Pair Distribution Function Measurements. *J. Appl. Crystallogr.* **2014**, *47*, 95–101.
- (19) Petkov, V. RAD, a Program for Analysis of X-ray Diffraction Data From Amorphous Materials for Personal Computers. *J. Appl. Crystallogr.* **1989**, *22*, 387–389.
- (20) Billinge, S. J. L.; Farrow, C. L. Towards a Robust ad hoc Data Correction Approach that Yields Reliable Atomic Pair Distribution Functions from Powder Diffraction Data. *J. Phys.: Condens. Matter* **2013**, *25*, 454202.
- (21) Jiang, T.; Mowbray, D. J.; Dobrin, S.; Falsig, H.; Hvolbæk, B.; Bligaard, T.; Nørskov, J. K. Trends in CO Oxidation Rates for Metal Nanoparticles and Close-Packed, Stepped, and Kinked Surfaces. *J. Phys. Chem. C* **2009**, *113*, 10548–10553.
- (22) Michaelides, A.; Liu, Z.-P.; Zhang, C. J.; Alavi, A.; King, D. A.; Hu, P. Identification of General Linear Relationships between Activation Energies and Enthalpy Changes for Dissociation Reactions at Surfaces. *J. Am. Chem. Soc.* **2003**, *125*, 3704–3705.
- (23) Nørskov, J. K.; Bligaard, T.; Logadottir, A.; Bahn, S.; Hansen, L. B.; Bollinger, M.; Bengard, H.; Hammer, B.; Slijvančanin, Z.; Mavrikakis, M.; Xu, Y.; Dahl, S.; Jacobsen, C. J. H. Universality in Heterogeneous Catalysis. *J. Catal.* **2002**, *209*, 275–278.
- (24) Zambelli, T.; Barth, J. L.; Wintterlin, J.; Ertl, G. Complex Pathways in Dissociative Adsorption of Oxygen on Platinum. *Nature* **1997**, *390*, 495–497.
- (25) Pauling, L. Factors Determining the Average Atomic Volumes in Intermetallic Compounds. *Proc. Natl. Acad. Sci. U.S.A.* **1987**, *84*, 4754–4756.
- (26) Pauling, L. *The Nature of the Chemical Bond*; Cornell University Press: Ithaca, 1975.
- (27) Rajasekharan, T.; Seshubai, V. Charge transfer on the metallic atom-pair bond, and the crystal structures adopted by intermetallic compounds. *Acta Crystallogr.* **2012**, *68*, 156–165.
- (28) Tao, F.; Grass, M. E.; Zhang, Y.; Butcher, D. R.; Renzas, J. R.; Liu, Z.; Chung, J. Y.; Mun, B. S.; Salmeron, M.; Somorjai, G. A. Reaction-Driven Restructuring of Rh-Pd and Pt-Pd Core–Shell Nanoparticles. *Science* **2008**, *322*, 932–934.
- (29) Tao, F.; Dag, S.; Wang, L.-W.; Liu, Z.; Butcher, D. R.; Bluhm, H.; Salmeron, M.; Somorjai, G. A. Break-up of Stepped Platinum Catalyst Surfaces by High CO Coverage. *Science* **2010**, *327*, 850–853.
- (30) Petkov, V.; Wanjala, B. N.; Loukrakpam, R.; Luo, J.; Yang, L.; Zhong, C. J.; Shastri, S. Pt–Au Alloying at the Nanoscale. *Nano Lett.* **2012**, *12*, 4289–4299.
- (31) Lu, G.-Y.; Henkelman, G. Role of Geometric Relaxation in Oxygen Binding to Metal Nanoparticles. *J. Phys. Chem. Lett.* **2011**, *2*, 1237–1240.
- (32) Zhang, L.; Anderson, R. M.; Crooks, R. M.; Henkelman, G. Correlating Structure and Function of Metal Nanoparticles for Catalysis. *Surf. Sci.* **2015**, *640*, 65–72.
- (33) Liu, H.; An, W.; Li, Y.; Frenkel, A. I.; Sasaki, K.; Koenigsmann, Ch.; Su, D.; Anderson, R. M.; Crooks, R. M.; Adzic, R. R.; Liu, P.; Wong, S. S. In situ Probing of the active Site Geometry of Ultrathin Nanowires for the Oxygen Reduction Reaction. *J. Am. Chem. Soc.* **2015**, *137*, 12597–12609.
- (34) Seraj, S.; Kunal, P.; Li, H.; Henkelman, G.; Humphrey, S. M.; Werth, C. J. PdAu Alloy Nanoparticle Catalysts: Effective Candidates for Nitrite Reduction in Water. *ACS Catal.* **2017**, *7*, 3268–3276.
- (35) Petkov, V.; Billinge, S. J. L.; Vogt, T.; Ichimura, A. S.; Dye, J. L. Structure of Intercalated Cs in Zeolite ITQ-4: an array of Metal Ions and Correlated Electrons Confined in a Pseudo-1D Nanoporous Host. *Phys. Rev. Lett.* **2002**, *89*, 075502.
- (36) Moore, W. J.; Pauling, L. The Crystal structures of the Tetragonal Monoxides of Lead, Tin, Palladium, and Platinum. *J. Am. Chem. Soc.* **1941**, *63*, 1392–1394.
- (37) van Spronsen, M. A.; Frenken, J. W. M.; Groot, I. M. N. Observing the Oxidation of Platinum. *Nat. Commun.* **2017**, *8*, 429.
- (38) Kepp, K. P. A Quantitative Scale of Oxophilicity and Thiophilicity. *Inorg. Chem.* **2016**, *55*, 9461–9470.
- (39) Mott, D.; Luo, J.; Njoki, P. N.; Lin, Y.; Wang, L.; Zhong, C. J. Synergistic Activity of Gold-Platinum Alloy Nanoparticle Catalysts. *Catal. Today* **2007**, *122*, 378–385.
- (40) Gao, H.; Xu, W.; He, H.; Shi, X.; Zhang, X.; Tanaka, K.-i. DRIFTS Investigation and DFT Calculation of the Adsorption of CO on Pt/TiO₂, Pt/CeO₂ and FeO_x/Pt/CeO. *Spectrochim. Acta, Part A* **2008**, *71*, 1193–1198.
- (41) Cheah, S. K.; Bernardet, V. P.; Franco, A. A.; Lemaire, O.; Gelin, P. Study of CO and Hydrogen Interactions on Carbon-Supported Pt Nanoparticles by Quadrupole Mass Spectrometry and Operando Diffuse Reflectance FTIR Spectroscopy. *J. Phys. Chem. C* **2013**, *117*, 22756–22767.
- (42) Lentz, C.; Jand, S. P.; Melke, J.; Roth, C.; Kaghazchi, P. DRIFTS Study of CO Adsorption on Pt Nanoparticles Supported by DFT calculations. *J. Mol. Catal. A: Chem.* **2017**, *426*, 1–9.
- (43) Fantauzzi, D.; Mueller, J. E.; Sabo, L.; van Duin, A. C. T.; Jacob, T. Surface Buckling and Subsurface Oxygen: Atomistic Insights into the Surface Oxidation of Pt(111). *ChemPhysChem* **2015**, *16*, 2797–2802.
- (44) Kale, M. J.; Christopher, P. Utilizing Quantitative in situ FTIR Spectroscopy to Identify Well-Coordinated Pt atoms as the Active Site for CO Oxidation on Al₂O₃ Supported Pt Catalysts. *ACS Catal.* **2016**, *6*, 5599–5609.
- (45) Raskó, J. CO-Induced Surface Structural Changes of Pt on Oxide-Supported Pt Catalysts Studied by DRIFTS. *J. Catal.* **2003**, *217*, 478–486.
- (46) Singh, J.; Nachtegaal, M.; Alayon, E. M. C.; Stötzel, J.; van Bokhoven, J. A. Dynamic Structure Changes of a Heterogeneous Catalyst within a Reactor: Oscillations in CO Oxidation over a Supported Platinum Catalyst. *ChemCatChem* **2010**, *2*, 653–657.
- (47) Chandler, B. D.; Pignolet, L. H. DRIFTS Studies of carbon Monoxide Coverage on highly Dispersed bimetallic Pt-Cu and Pt-Au Catalysts. *Catal. Today* **2001**, *65*, 39–50.
- (48) Hendriksen, B. L. M.; Frenken, J. W. M. CO Oxidation on Pt(110): Scanning Tunneling Microscopy Inside a High-Pressure flow Reactor. *Phys. Rev. Lett.* **2002**, *89*, 046101.
- (49) Grass, M. E.; Zhang, Y.; Butcher, D. R.; Park, J. Y.; Li, Y.; Bluhm, H.; Bratlie, K. M.; Zhang, T.; Somorjai, G. A. A Reactive Oxide Overlayer on Rhodium Nanoparticles During CO Oxidation and its Size Dependence Studied by in situ Ambient-Pressure X-ray Photoelectron Spectroscopy. *Angew. Chem.* **2008**, *120*, 9025–9028.
- (50) Singh, J.; Alayon, E. M. C.; Tromp, M.; Safonova, O. V.; Glatzel, P.; Nachtegaal, M.; Frahm, R.; van Bokhoven, G. A. Generating Highly Active Partially Oxidized Platinum during Oxidation of Carbon

Monoxide over Pt/Al₂O₃: In Situ, Time-Resolved, and High-Energy-Resolution X-Ray Absorption Spectroscopy. *Angew. Chem.* **2008**, *120*, 9400–9404.

(51) Lu, A.; Peng, D.-L.; Skeete, Z.; Yan, S.; Kareem, H.; Shan, S.; Chang, F.; Chen, Y.; Zheng, H.; Zeng, D.; Yang, L.; Jenkins, D. M.; Sharma, A.; Luo, J.; Petkov, V.; Zhong, C. J. From a Au-rich core/PtNi-rich shell to a Ni-rich core/PtAu-rich shell: an effective thermochemical pathway to nanoengineering catalysts for fuel cells. *J. Mater. Chem. A* **2018**, *6*, 5143–5155.

(52) Shan, S.; Kareem, H.; Luo, J.; Maswadeh, Y.; Petkov, V.; Zhong, C. J. Manuscript in progress.